DOI:
10.1016/j.rse.2017.02.024

Document Version
Publisher's PDF, also known as Version of record

Remote Sensing of Environment 193 (2017) 138–149

Contents lists available at ScienceDirect

Remote Sensing of Environment

journal homepage: www.elsevier.com/locate/rse

Major advances in geostationary fire radiative power (FRP) retrieval over Asia and Australia stemming from use of Himarawi-8 AHI

Weidong Xu [a,b], Martin J. Wooster [a,b,*], Takayuki Kaneko [c], Jiangping He [a], Tianran Zhang [a,b], Daniel Fisher [a,b]

[a] King's College London, Department of Geography, Strand, London WC2R 2LS, UK
[b] NERC National Centre for Earth Observation (NCEO), UK
[c] Earthquake Research Institute, University of Tokyo, 1-1-1 Yayoi, Bunkyo-ku, Tokyo 113-0032, Japan

ARTICLE INFO

Article history:
Received 30 May 2016
Received in revised form 20 February 2017
Accepted 28 February 2017
Available online xxxx

Keywords:
Biomass burning
Fire radiative power
Himawari-8
Geostationary

ABSTRACT

Characterising the highly variable temporal dynamics of landscape-scale fire activity is best achieved using geostationary satellites, and the Himawari-8 Advanced Himawari Imager (AHI) now provides views of Asian and Australian fires at an unprecedented 10 min temporal resolution and 2 km nadir thermal channel spatial resolution. We here develop the first processing system to identify active fires and retrieve their fire radiative power (FRP) from AHI data, based on the geostationary Fire Thermal Anomaly (FTA) algorithm and FRP retrieval method originally developed for use with Meteosat SEVIRI over Africa and Europe. This scheme detects active fires covering as little as 10^{-3} to 10^{-4} of an AHI pixel, and we compare performance to the same scheme applied to data from the forerunner geostationary MTSAT imager and the FengYun-2 (FY-2) Stretched Visible and Infrared Spin Scan Radiometer (S-VISSR), and also to 1 km (at nadir) polar-orbiting MODIS active fire data. We find major benefits of Himawari-8 AHI over both MTSAT and FY-2, being able to detect a substantially greater proportion of fire activity and with little impact from sensor saturation. AHI-derived FRP retrievals of detected fires show a very strong agreement and a low (3 MW) bias with respect to near-simultaneous MODIS retrievals, though fires having FRP ≤ 40 MW are undercounted by AHI due to its 4× larger pixel area (at nadir) than MODIS. Large parts of Asia are characterised by smaller/lower FRP fires associated with e.g. agricultural residue burning, meaning many are at or below this AHI minimum FRP detection limit, and during June 2015 AHI fails to detect around 66% of the hotspots that MODIS detects when both sensors view the same area simultaneously. However, AHI provides 144 observation opportunities per day compared to 4 typical observations from MODIS, and shows a low (8%) active fire detection error of commission. We demonstrate the unique value of the geostationary FRP retrievals made from AHI data for full fire diurnal cycle assessment and for Fire Radiative Energy (FRE) calculations. We conclude that these FRP data demonstrate major benefits for studies of active fires over Asia and Australia, and expect them to become an important component of the global geostationary active fire observation system.

1. Introduction

Landscape fires are frequent across much of Asia and Australia, and EO satellites are vital to assessing their terrestrial and atmospheric impacts in this globally important biomass burning region (e.g. Williams et al., 1998; Wooster et al., 2012; Li et al., 2016). Many fires in Asia are associated with agricultural residue burning and/or tropical forest degradation and deforestation, and are often individually small and so quite difficult to detect via moderate spatial resolution burned area mapping approaches. Active fire products offer improved sensitivity to such 'small' fires (Roy et al., 2008), though the typically short-lived nature of agriculgtural residue burning fires still poses a challenge, and such observations can be accompanied by retrievals of a fires radiative power (FRP) output that relates directly to its fuel consumption and smoke emission (e.g. Wooster et al., 2005). Here we develop for the first time a new very high temporal resolution capability for active fire detection and FRP characterisation over Asia and Australia, using the first of a new generation of geostationary Earth imaging satellites - Himawari-8 (Bessho et al., 2016; Kurihara et al., 2016; JMA, 2014), which will be followed by the Geostationary Operational Environmental Satellite-R Series (GOES-R) over the America's and by Meteosat Third Generation (MTG) over Africa and Europe. We demonstrate the significant advantages of this new technology for active fire characterisation and FRP assessment, evaluating performances against near-simultaneously acquired MODIS active fire data available a few times per day over the same regions.

Geostationary active fire detection has previously been provided over Asia and Australia using the Japanese Multifunctional Transport

* Corresponding author at: King's College London, Department of Geography, Strand, London WC2R 2LS, UK.
E-mail address: martin.wooster@kcl.ac.uk (M.J. Wooster).

http://dx.doi.org/10.1016/j.rse.2017.02.024

Satellite (MTSAT) imager and the Korean Communication, Ocean and Meteorological Satellite (COMS) (Zhang et al., 2012), though FRP assessment has typically not been available. Himawari-8 offers potential for much improved performance due to its enhanced sensor characteristics, and we use an adaptation of the geostationary Fire Thermal Anomaly (FTA) algorithm of Wooster et al. (2015) to provide this capability, applying the same FTA algorithm to data from MTSAT and the Chinese FengYun-2 (FY-2) geostationary satellite for comparison. We compare results from each system to those from MODIS, and briefly explore the landscape fire characteristics of a variety of key biomes in Asia and Australia using these new active fire data, pointing the way to what the forthcoming GOES-R system in particular should deliver over the Americas from 2017.

2. Asian and Australian fire activities and the potential of geostationary data

Fires in Asia and Australia appear responsible for around a quarter to a third of annual global burned area (Giglio et al., 2006; Van der Werf et al., 2010), resulting from e.g. annual savannah and forest fires in Australia (Stephenson et al., 2013), the burning of agricultural residues across much of Asia (e.g. Zhang et al., 2012; Zhang et al., 2015 and Li et al., 2016), and fires in drained peatlands and often already degraded forests in SE Asia that show particular activity peaks during El Niño-related droughts (Van der Werf et al., 2004; Van der Werf et al., 2010; Huijnen et al., 2016). This fire activity affects landcover and terrestrial ecosystem functioning, contributes significantly to modification of the regional atmosphere, and can impact concentrations of atmospheric greenhouse gases in globally significant ways (Bowman, 2000; Johnston et al., 2011; Reid et al., 2013; Huijnen et al., 2016).

Landscape fires are highly dynamic, often changing their nature in a matter of minutes and typically showing very strong diurnal cycles (Giglio, 2007; Roberts et al., 2009a). Such details can only be directly revealed from geostationary satellites, which provide multiple observations every hour that enable identification of even short-lived fires provided they are not too small to be detected, full fire radiative energy (FRE) characterisation over the diurnal cycle, and better recognition of fires burning in cloudy areas since cloud gaps can be fully exploited (e.g. Roberts et al., 2005; Roberts and Wooster, 2008). Using Meteosat data of Africa and Europe, the value of geostationary FRP information for fire emissions and smoke plume transport modelling has been demonstrated by Wooster et al. (2005), Roberts et al. (2005); Baldassarre et al. (2015) and Roberts et al. (2015), and for fire diurnal cycle assessment and characterisation by e.g. Roberts et al. (2009a). However, even when using detection algorithms capable of identifying fires covering as little as 10^{-4} of a pixel (Roberts et al., 2005; Wooster et al., 2015), a limitation of geostationary active fire remote sensing has been its inability to detect the lowest FRP fires due to the typically large pixel areas involved (Roberts and Wooster, 2008; Hyer et al., 2013). However, new generations of geostationary satellites offer increasing spatial fidelity, reducing the importance of this issue over time and offering the best opportunity to detect fires at an early stage via their high imaging frequency (Roberts et al., 2015).

3. Geostationary satellites operating over Asia and Australia

3.1. MTSAT and Himawari-8

MTSAT carrying the MTSAT Imager was operated from 2008 to 2015 by the Japan Meteorological Agency (JMA) over the equator at 140° East. Himawari-8 is the first of the third generation of geostationary weather satellites, launched on 7th October 2014 carrying the new AHI instrument to replace MTSATs capability. We used Himawari-8 AHI data from June 2015, the month when agricultural fire activity in eastern China typically peaks and fire activity in South Asia and Australia starts to intensify (Zhang et al., 2012; Li et al., 2016; Chand et al., 2007; Williams et al., 1998).

Prior to Himawari-8 AHI, the MTSAT imager provided 10-bit, full disk imagery at half past every hour in five spectral bands at a spatial sampling distance of 1 km (visible channel) and 4 km (Infrared channels) at the sub-satellite point (SSP) (Table 1), along with a half disk (northern hemisphere) image every hour. Himawari-8 AHI significantly improves on this, providing full disk 10-bit, radiometrically and geometrically calibrated data in 16 spectral channels every 10 min, with the potential updates every minute over sub-regions (Bessho et al., 2016). Fig. 1 shows an example AHI full disk colour composite image, along with detail over fires in northern Australia. We were not able to access MTSAT data of June 2016, so we instead used Feb. 2009 to coincide with the Australian 'Black Saturday bushfires' and the date of the FengYun-2 satellite data discussed next.

3.2. FengYun-2

FengYun-2 (FY-2) is the first generation of Chinese geostationary spin stabilized meteorological satellite (Guo et al., 2009), and carries the five channel Stretched Visible and Infrared Spin Scan Radiometer (S-VISSR) operating at an SSP spatial sampling distance of 1.25 km for the visible band and 5 km for the thermal infrared channels (Table 1). S-VISSR provides a single full disk, 8-bit image every hour, and Fig. 2 shows a rendition of near simultaneous FY-2 and MTSAT imagery.

4. FTA algorithm application to Asian geostationary satellites

To detect active fire pixels we use the geostationary Fire Thermal Anomaly (FTA) algorithm (Roberts and Wooster, 2008) and the MIR radiance FRP retrieval method (Wooster et al., 2003), originally designed for use with Meteosat SEVIRI (Wooster et al., 2005; Roberts et al., 2005), and now used to generate the real-time Meteosat FRP-PIXEL products within the EUMETSAT Land Surface Analysis Satellite Application Facility (LSA SAF; Wooster et al., 2015). The active fire detection and FRP characterization process occurs over three stages: Firstly, identification of pixels having signals suggestive of actively burning fires; secondly a more detailed contextual set of multi-spectral tests used to confirm whether or not these 'potential fire pixels' do indeed contain fires; and thirdly derivation of atmospherically corrected FRP estimates and associated uncertainties for each confirmed active fire pixel. Full algorithm details are provided in Roberts and Wooster (2008) and Wooster et al. (2015). Since AHI has a higher spatial resolution than SEVIRI, and slightly different waveband coverage, certain of the FTA algorithm thresholds required optimization use with Himawari-8. The initial thresholds were checked for suitability via visual inspection of the output and comparison to MODIS active fire detections. Thresholds were adjusted to maximize detection of true fires while minimizing false alarms, as per Roberts and Wooster (2008) and Wooster et al. (2015). Application of the FTA algorithm to MTSAT and FY-2 proceeded similarly, and all adaptations were found relatively straightforward, as was previously the case when using the FTA with GOES-E and -W data (Xu et al., 2010). Unlike Meteosat, neither Himawari-8, MTSAT nor FY-2 data come with a dedicated cloud mask, so we adapted the image based cloud masking procedure described in Xu et al. (2010). Finally, the power law scaling coefficient a ($mW \cdot m^{-2} \cdot sr^{-1} \cdot (cm^{-1})^{-1} \cdot K^{-4}$) used in the FRP retrieval algorithm for each sensor (Eq. 1) was calculated according to Wooster et al. (2005), and the MWIR band atmospheric transmission (τ_{MIR}) calculated according to Wooster et al. (2015).

$$FRP_{MIR} = \frac{A_{samp}\sigma\varepsilon}{a\varepsilon_{MIR}}\left(\frac{L_{MIR}}{\tau_{MIR}}\right) \quad (1)$$

where A_{samp} is the pixel sampling area (m^2), σ is Stefan-Boltzman constant (5.67E-8 $Js^{-1} \cdot m^{-2} \cdot K^{-4}$), ε is the fire emissivity and ε_{MIR} the spectral emissivity in the MIR (and fires are assumed to be grey bodies so

Table 1
Basic characteristics of the imagers carried by Himawari-8, MTSAT and FY-2. Notice only the channels used herein are listed, alongside their use in the active fire detection and characterization algorithm.

Satellite & imager	Spectral channel	Wavelength range (μm)	Spatial sampling distance at SSP (km)	Primary use in active fire detection & FRP derivation scheme
Himawari-8 AHI	3	0.63–0.66	0.5	Cloud masking
	7	3.74–3.96	2	Active fire detection & FRP derivation (MWIR band saturates at high BT of 400 K)
	14	11.1–11.3	2	Active fire detection
MTSAT Imager	1	0.55–0.80	1	Cloud masking
	2	10.3–11.3	4	Active fire detection
	5	3.5–4.0	4	Active fire detection & FRP derivation (though MWIR band saturates at relatively low BT of 320 K, leading to extensive saturation over even warm backgrounds).
FY-2 S-VISSR	1	0.55–0.75	1.25	Cloud masking
	2	10.3–11.3	5	Active fire detection
	4	3.5–4.0	5	Active fire detection & FRP derivation (MWIR band saturates at moderate temperature of 340 K).

that $\varepsilon = \varepsilon_{MIR}$), and L_{MIR} is the contribution of the fire to the total MWIR band spectral radiance of the active fire pixel ($mW \cdot m^{-2} \cdot sr^{-1} \cdot (cm^{-1})^{-1}$).

5. Asian geostationary FTA algorithm evaluation

5.1. Methodology

Our performance evaluation of the resulting geostationary active fire datasets was based on comparison to MODIS Collection 5 MOD14 and MYD14 active fire products from the Terra and Aqua satellites (Giglio et al., 2003). With a nadir spatial resolution of 1 km, MODIS is capable of detecting sub-pixel sized fires having an FRP significantly lower than the minimum detectable from geostationary imagers (Roberts et al., 2015). We followed the intercomparison procedure recently used between MODIS and the LSA SAF Meteosat SEVIRI FRP-PIXEL product (Roberts et al., 2015), making comparisons only when data were collected within ±6 min of one other and within a MODIS scan angle of ±30° to limit MODIS' pixel area growth to a factor of ~1.7 compared to nadir (Freeborn et al., 2011, 2014).

5.1.1. Active fire detection evaluation methodology

Following Roberts et al. (2015), MODIS imagery and active fire data were first spatially remapped to the relevant geostationary imaging grids to deal with the varying pixel sizes (Wolf and Just, 1999), and if two or more MODIS active fire pixels fell within one grid cell their FRP values were summed. The original MODIS imagery aided interpretation, and the remapped MODIS active fire data (termed here MODIS-R) were quantitatively compared to the geostationary data, with active fire detection errors of omission occurring when a MODIS-R grid cell containing at least one active fire pixel was matched to a location imaged within ±6 min by the geostationary sensor but which showed no actual geostationary fire detection within a 5×5 pixel window (Freeborn et al., 2014). Geostationary errors of commission occurred when an actually detected geostationary active fire pixel had no matching MODIS-R active pixel within the corresponding 5×5 pixel window.

Fig. 3 indicates the methodology applied to a single matched AHI and MODIS subscene of China. Comparison of Fig. 3d and e demonstrates that certain active fires detected in the MODIS data fail to be detected by the lower spatial resolution AHI data, but that many other fires are successfully identified in both. Overall, in this example, MODIS detects 1246 active fire pixels, equivalent to 859 MODIS-R pixels after remapping to the AHI grid. Among these 859 remapped fire pixels, 602 (~70%) had no corresponding AHI detection in the matching 5×5 window, an error of omission very similar to the 73% reported recently for the Meteosat SEVIRI FRP-PIXEL product that uses the same FTA detection algorithm (Roberts et al., 2015). This is reasonable performance given that the fire affected region of Fig. 3 is quite far from the AHI subsatellite point and thus has a ground pixel area around 4× to 8× larger than MODIS, depending on MODIS scan angle. At the same time, AHI detected 162 individual active fire pixels, with 152 (~94%) having a corresponding MODIS active fire pixel, demonstrating a low (6%) false alarm/error of commission rate. Results akin to those from this single matchup scene were accumulated across one month of data from each geostationary sensor (June 2015 for Himawari, Feb.2009 for MTSAT and FY-2).

For Himawari-8 AHI, the June 2015 full disk imagery included fires mainly located in China, Thailand, Indonesia and Australia. For the MTSAT and FY-2 evaluation, the full disk Feb. 2009 data saw fires across

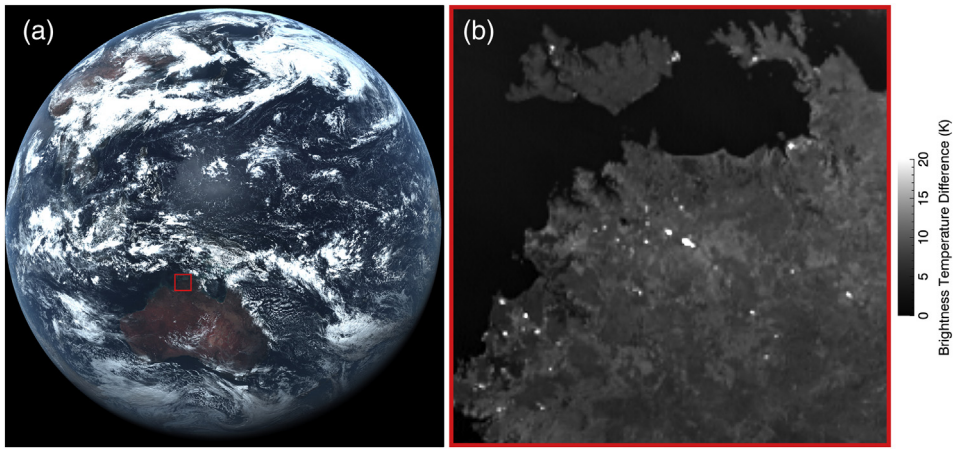

Fig. 1. Example data from the Himawari-8 Advanced Himawari Imager (AHI), collected at 03:00 UTC on 7th June 2015. (a) Colour composite full disk image (RGB = AHI Channels 3, 2, 1), and (b) subset of northern Australia highlighted in (a) and shown as the difference between the recorded MWIR and LWIR brightness temperatures (Channels 7 and 14; Table 1) so that pixels containing sub-pixel active fires are highlighted as high values, as explained in Xu et al. (2010) and Wooster et al. (2013, 2015). Areal coverage of actively burning fires down to sizes of 10^{-3} to 10^{-4} of a pixel typically increase this BT difference metric to 5–10 K or greater, which is generally sufficient to enable active fire detection to occur (Wooster et al., 2005).

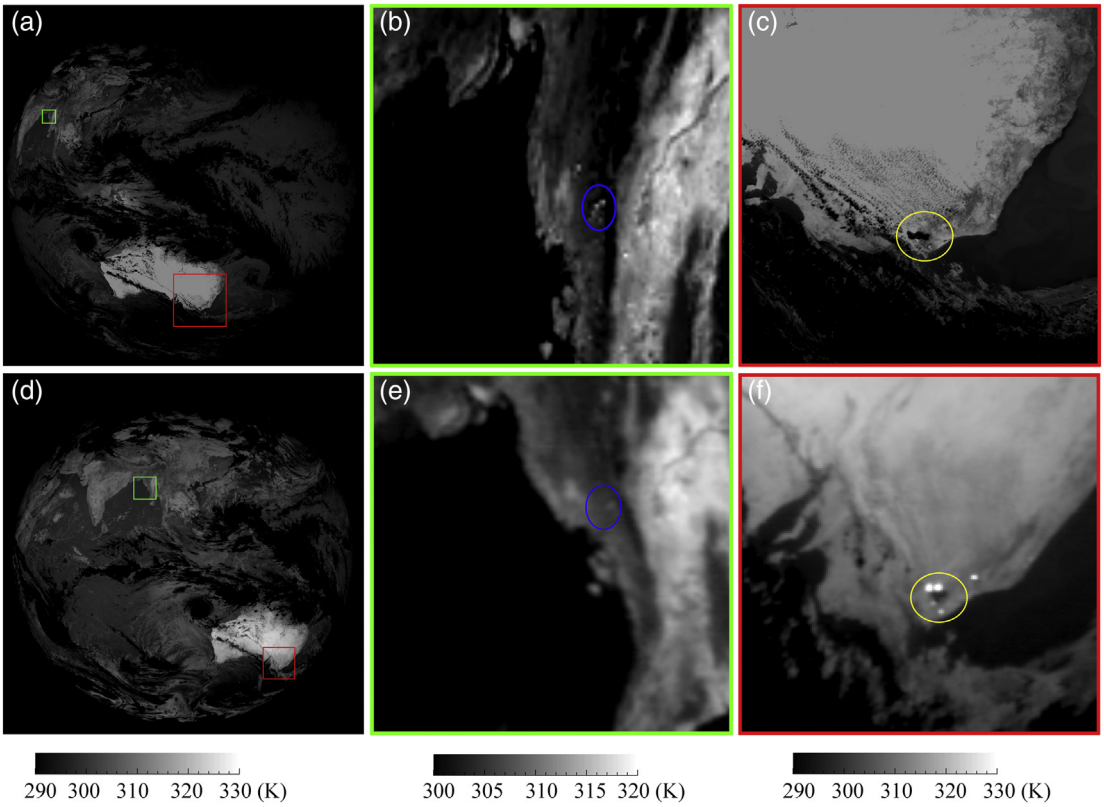

Fig. 2. Near simultaneous MWIR brightness temperature imagery from the MTSAT imager (top row) and FY-2 S-VISSR imager (bottom row), collected on 7th February 2009. (a) Full disk MTSAT image (5:30 UTC) with areas in Australia and Myanmar highlighted in red and green respectively; (b) MTSAT sub-image over Myanmar outlined in (a) where a few fires are circled in blue are visible but which are not apparent in the almost simultaneous FY-2 VISSR imagery shown in (e); (c) MTSAT sub-image covering parts of New South Wales and Victoria (Australia) during the 'Black Saturday bushfires' (circled in yellow) – of which only a small part can be discerned due to MWIR channel saturation affecting large areas; (d) full disk FY-2 S-VISSR scene collected at 5:00 UTC; (e) S-VISSR sub-image outlined by the green rectangle in (d) and matching the MTSAT sub-image in (c); (f) S-VISSR sub-image covering parts of New South Wales and Victoria of Australia matching the MTSAT sub-image shown in (c) and where the 'Black Saturday bushfires' do appear as a group of high MWIR BT pixels circled in yellow. (For interpretation of the references to colour in this figure legend, the reader is referred to the web version of this article.)

parts of Australia and Thailand. It was not possible to directly intercompare MTSAT and FY-2 active fire detection outputs on a point-by-point basis, because of the different imaging times of each system – further supporting use of the MODIS active fire detection data as the standard against which the geostationary sensors are assessed. The number of MOD14/MYD14 products matching within ±6 min of each Asian geostationary satellite dataset, and which of these had active fires present within them, are listed in Table 2. Of course, since landscape burning is highly dynamic, active fire detection performances typically vary somewhat across locations, times of day and season (e.g. Roberts and Wooster, 2008; Freeborn et al., 2014). The differences we report here between the errors of omission and commission of the three geostationary sensors are likely to be somewhat influenced by this, but our broad findings regarding the general performance are considered representative.

5.1.2. FRP evaluation methodology

Following the type of active fire pixel clustering procedure used in Zhukov et al. (2006), Roberts and Wooster (2008), Xu et al. (2010), we first compared the FRP recorded by Himawari-8 AHI to that recorded by MODIS on a 'per fire' basis, defined as a contiguous or near-contiguous group of active fire pixels detected near-simultaneously. MODIS retrievals were made using the same Wooster et al. (2003, 2005) MIR radiance approach as with the geostationary datasets (Eq. 1), which is now also used to generate MODIS' Collection 6 FRP data (Giglio et al., 2016). MODIS FRP was atmospherically corrected using the same procedure as with AHI (described in Wooster et al. (2015)).

Whilst per-fire comparisons between geostationary and MODIS FRP retrievals have previously reported low bias (e.g. Roberts and Wooster, 2008; Xu et al., 2010; Roberts et al., 2015), there typically remains significant regional-scale FRP underestimation because of the inability of geostationary data to detect the lowest FRP fires (e.g. Roberts and Wooster, 2008; Xu et al., 2010; Roberts et al., 2015). To assess this, the Himawari-8 and MTSAT active fire data were subset to cover the same geographic area as each MODIS scene (within a ±30° MODIS scan angle) and each datasets total FRP compared to assess the importance of fires missed by the geostationary sensors but detected by MODIS.

5.2. Results

5.2.1. FY-2 evaluation

Taking FY-2 first, MODIS-R data contemporaneous with FY-2 showed 2035 active fire grid cells, but only 9 were matched by active fire pixels detected by FY-2, indicating a near total failure by FY-2 to detect them (Table 3). Such a high omission error rate results from a combination of the S-VISSR sensors lower spatial resolution and decreased radiometric sensitivity compared to the MTSAT imager and Himawari-8 AHI (as well as compared to MODIS), and the apparently relatively poor quality of the S-VISSR MWIR spectral band measurements (see Fig. 2).

FY-2 S-VISSR does have a better vantage point for observing certain Asian-Pacific areas compared to MTSAT, due to its orbital position (e.g. the region of Myanmar highlighted in green, where FY-2 has pixel spatial sampling distance of ~5.4 km and MTSAT ~6 km, Fig. 2). Nevertheless, MTSAT often appears to better identify actively burning fires than FY-2 even in such areas (e.g. compare Fig. 2b showing MTSAT with the near simultaneous FY-2 S-VISSR imagery of Fig. 2e). However, where large fires and high ambient background temperatures lead to

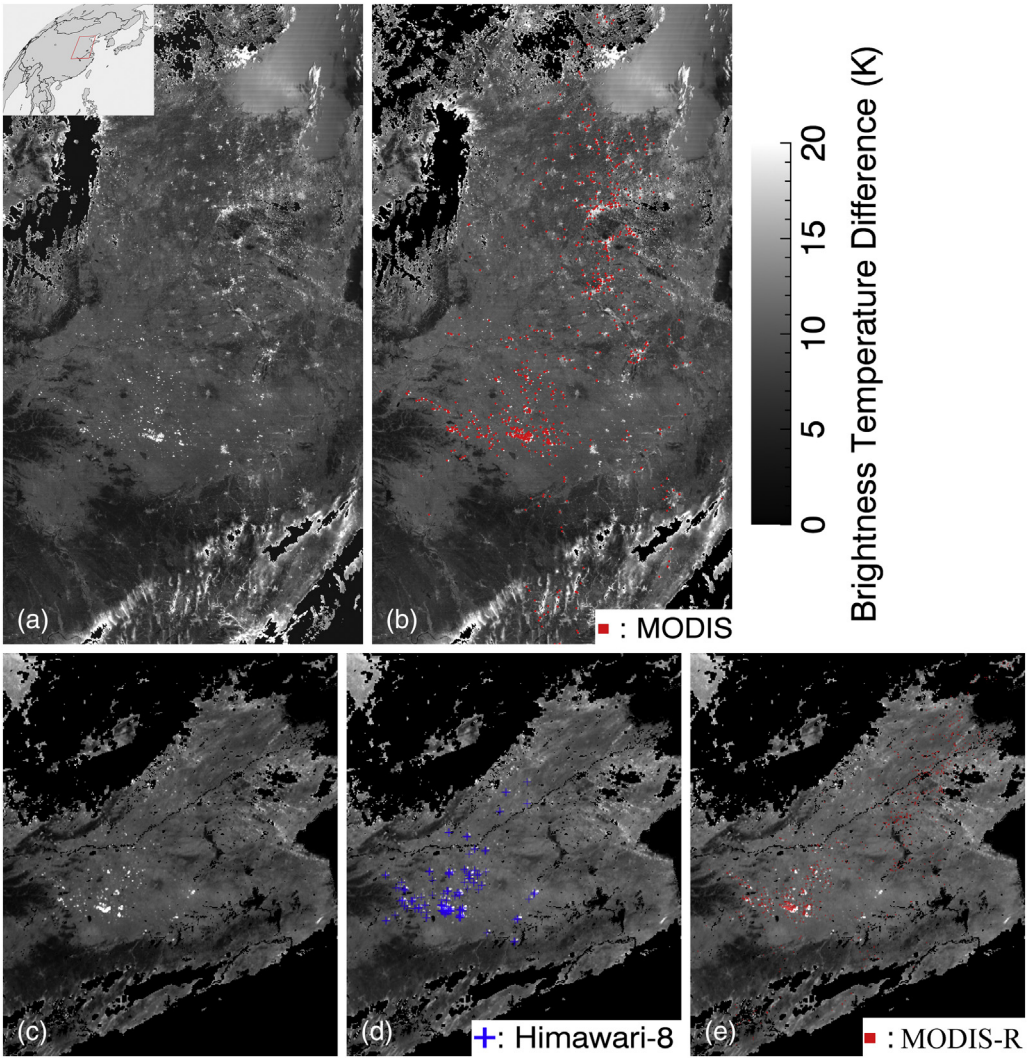

Fig. 3. Example methodology used for geostationary active fire detection performance evaluation. Here, Himawari-8 AHI data and matching MODIS data are shown over China (03:10 UTC on 11th June 2015; for location see top left inset). (a) MODIS MWIR-LWIR Band Brightness temperature (BT) difference image, and (b) matching active fire detections (red) superimposed with a one pixel offset for clarity. Areas of cloud and standing water are masked out in these MODIS subscenes. (c) and (d) show from Himawari-8 the same MWIR-LWIR BT difference metric (now calculated using the AHI imagery), along with the corresponding AHI-detected active fire detections (blue). (e) MODIS active fire detections made within a ±30° MODIS scan angle (red), mapped to the AHI image projection. (For interpretation of the references to colour in this figure legend, the reader is referred to the web version of this article.)

saturation of the MTSAT MWIR spectral band FY-2 can still show some advantage. An example is during the extreme 'Black Saturday bushfires' that burned intensely across the Australian state of Victoria on 7th February 2009 (Engel et al., 2013). Clearly seen in FY-2 data, albeit appearing somewhat 'blurred' (Fig. 2f), in MTSAT they appear far less clearly (circled yellow in Fig. 2c). This results from the comparatively low 320 K saturation temperature of the MTSAT MWIR band (Channel 5; Table 1). Due to the high environmental temperatures seen at this time, MTSAT Channel 5 saturation is occurring over many of the background pixels as well as almost all the fire pixels, severely hampering discrimination of the latter. This is not the case with FY-2 S-VISSR, and Fig. 4 shows a comparison between the FRP timeseries from MODIS, FY-2 and MTSAT, where the latter shows a particular inability to detect these large fires during much of the day (as in Fig. 2c). However, though FY-2 can detect the fires after ~11:00 h local solar time, their FRP retrieval closest to the ~14:00 h daytime MODIS overpass is only around one third of that of MODIS, again partly due to MWIR band saturation - but in the case of S-VISSR only over the fires themselves (Fig. 4).

Table 2
Number of Collection 5 MOD14 and MYD14 active fire products used in comparisons to our Himawari-8 AHI, MTSAT and FY-2 active fire data.

	Himawari-8	MTSAT	FY-2
MODIS products coincident with the geostationary data (±6 min)	4243	672	664
MODIS products coincident with the geostationary data (±6 min) and in which the MODIS products showed the presence of active fires	204	58	34

Table 3
Active fire detection errors of omission and commission for the FTA algorithm applied to Himawari-8 AHI, MTSAT imager and FY-2 S-VISSR data, calculated via comparison to near-simultaneous MODIS active fire pixels detected (MOD14 and MYD14).

Asian geostationary satellite	Himawari-8	MTSAT	FY-2
No. of fire pixels present at times coincident with a MODIS overpasses	1974	140	8
Fire pixels detected by MODIS at these times	1825	124	6
Geostationary active fire detection error of commission	8%	11%	25%
No. of MODIS fire pixels	12,229	3279	3468
No. of MODIS fire pixels after remapped to geostationary projection	8575	1830	2035
No. of MODIS fire pixels after remap detected by geostationary satellite	2895	259	9
Geostationary active fire detection error of omission	66%	86%	99%

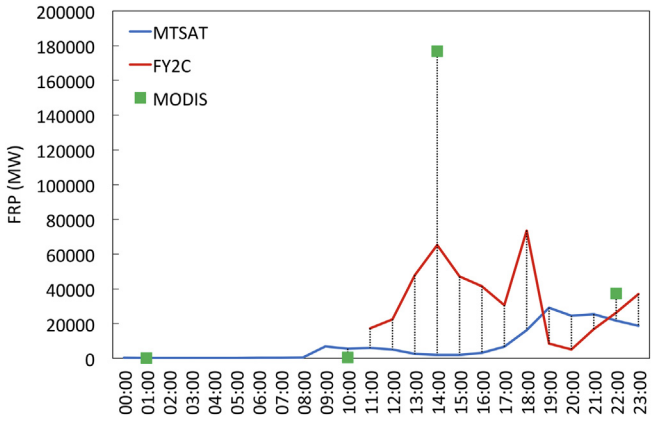

Fig. 4. FRP time series data of the Australian 'Black Saturday bushfires' for 7th Feb 2009. MTSAT and FY-2 show very significant FRP underestimation compared to the simultaneous MODIS observations, though with FY-2 performing in this case apparently better than MTSAT due to the latter's extreme levels of MWIR band saturation during the early afternoon diurnal fire peak (see main text). X-axis shows local solar time.

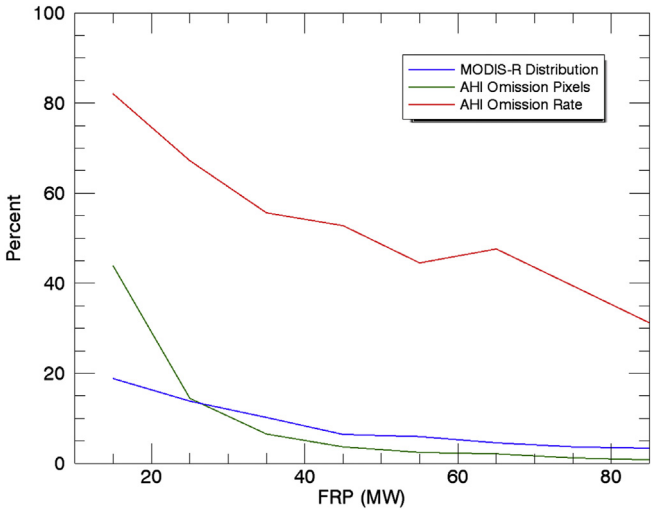

Fig. 5. Details of AHI active fire pixel omissions with respect to MODIS, binned into 10 MW intervals. Blue line shows the relative frequency (expressed as a percentage) of remapped MODIS (i.e. MODIS-R) pixels at each FRP level. Red line shows the percentage of MODIS-R pixels at each FRP level that remained undetected by AHI (i.e. the omission rate at that FRP value). Green line shows the relative importance of the undetected fire pixels at each FRP level, expressed as a percentage of the FRP of the total undetected fire pixel set. See main text for a full explanation of MODIS-R data. (For interpretation of the references to colour in this figure legend, the reader is referred to the web version of this article.)

After around 18:00 h, background brightness temperatures typically fall below 320 K in MTSAT's MWIR band, and MTSAT once again becomes preferable to use (Fig. 4). We conclude therefore that whilst FY-2 S-VISSR does offer some limited benefit for detection of very large fires burning in high ambient temperature conditions, in general they appear to be poorly suited to the active fire application and their use was not pursued further herein.

5.2.2. AHI and MTSAT active fire detection evaluation

Table 3 reports results of the active fire detection evaluation for both Himawari-8 AHI and the MTSAT imager. For the AHI, 66% of MODIS-R fire pixels made within the AHI full disk had no corresponding AHI-detected active fire pixel, an omission error higher than the 53–59% found when the FTA algorithm prototype was applied to limited amounts of Meteosat SEVIRI data (Roberts and Wooster, 2008), but lower than the 73% reported with the operational FTA algorithm (Roberts et al., 2015). Errors of omission rates differ over time for SEVIRI, due in part to different seasons (and thus fire affected areas and locations) being included in the comparisons. Those for AHI lie in between, though since the AHI ground pixel area at same view zenith angle is smaller than that of SEVIRI, the omission error for AHI might be expected to be lower. However, the domination of small (low FRP) agricultural residue burning fires across much of Asia provides a set of targets likely to be in general more difficult to detect than the larger grassland fires dominating much of Africa (Giglio et al., 2016; Li et al., 2016). Therefore, though the geostationary data do offer the advantage of capturing almost continuous imagery for better detection of short-lived agricultural residue fires, their typically low FRP can make them a challenge to detect if only a few are burning simultaneously in a particular AHI pixel. This is exacerbated here, because in June 2015 most of the fire-affected areas within the AHI disk are actually quite far from the sub-satellite point, resulting in increased AHI pixel areas and a higher minimum FRP detection limit compared to closer to nadir (see Fig. 10). Simultaneous AHI and MODIS data make it clear that AHI misses some fire pixels that MODIS can successfully detect, though Fig. 5 indicates that the AHI active fire detection omission rate decreases sharply with increasing FRP, being around 80% for MODIS-R active fire pixels of ~15 MW, around 50% at ~40 MW, and below 40% in excess of 80 MW. Performance beyond an FRP of 90 MW is not considered due to the limited number of high FRP MODIS-R fire pixels available.

Fig. 5 also shows the number of MODIS-R fire pixels coincident with an AHI image at each FRP level (expressed as a percentage of the entire MODIS-R coincident fire pixel set), along with the proportion AHI fails to detect (expressed as a percentage of the total number of omissions). MODIS-R fire pixels having an FRP of ~15 MW or less are those most commonly missed by AHI, comprising ~20% of the total MODIS-R fire pixel set, and as their aforementioned 80% omission rate attests to they represent a large proportion (45%) of the MODIS-R fire pixels that AHI fails to detect. As FRPs increase, those fire pixels omitted by AHI become a smaller fraction of the overall AHI omitted pixel set. These data confirm that the majority of active fire pixels that AHI misses but MODIS detects are 'small' low FRP fires, as would be expected from the formers larger (nadir) pixel area. Of course, other effects also impact the rate of omission, such as the quality and sensitivity of the cloud masks applied to each data type (Freeborn et al., 2014).

Fig. 6 displays the spatial distribution of AHI's errors of omission compared to MODIS-R using 0.5° grid cells. Because lower FRP fires dominate those missed (Fig. 5), the percentage of grid-cell MODIS-R fire counts that are missed by AHI (Fig. 6a) is typically higher than the percentage of the MODIS-R grid-cell FRP that these non-detections represent (Fig. 6b). AHI tends to miss higher proportions of MODIS-detected active fire pixels in areas where fires are less common and/or are more dominated by smaller/lower FRP events (e.g. in June 2015 in China, Indonesia and Thailand) and lower proportions in areas like Northern Australia where individual fires are larger and often burn more intensely.

In terms of active fire errors of commission, 8% of the AHI-detected active fire pixels had no matching MODIS detection, a similar commission error to the 6–8% reported using the FTA algorithm with Meteosat over Africa (Roberts and Wooster, 2008) and the 8% found with GOES across South America (Xu et al., 2010).

In terms of MTSAT, its active fire data show higher errors of omission (86%) and commission (11%) than Himawari-8 AHI, most likely reflecting the formers larger pixel area and thus lower sensitivity to active fires, and also the impact of MTAT's MWIR band saturation problem over warmer backgrounds (as discussed in Section 3.2 and shown in Fig. 2).

5.2.3. AHI and MTSAT FRP characterisation

5.2.3.1. Per-fire FRP intercomparison. Fig. 7 presents results of the per-fire AHI to MODIS FRP intercomparison, showing high correlation (r^2 = 0.98) and a slope of 0.99 for the linear-best fit. AHI shows a low bias of 3 MW compared to MODIS, a standard deviation of 156 MW (32%),

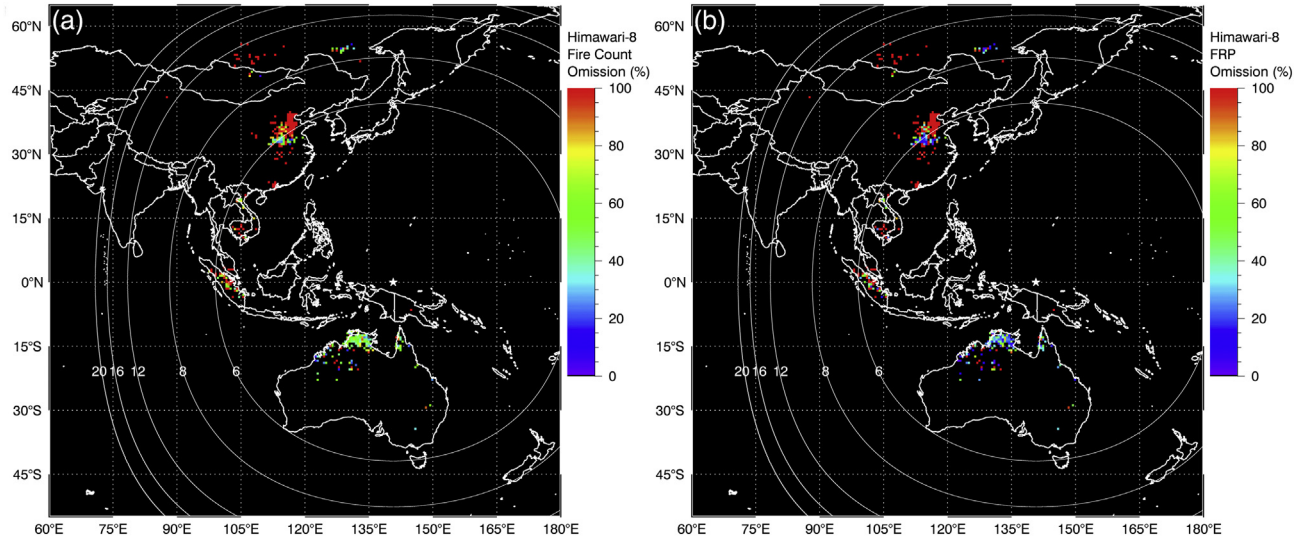

Fig. 6. Regional distribution (0.5° resolution) of Himawari-8 AHI active fire omissions relative to near simultaneous MODIS-R data. (a) Percentage of MODIS active fire pixels missed by AHI in each grid-cell, and (b) percentage of grid cell total FRP as measured by the MODIS-R data that is represented by fire pixels remaining undetected by AHI. AHI sub-satellite point is indicated by the white star above Papua New Guinea/West Papua, whilst white circles indicate contours of AHI pixel area (labels are area in km^2).

and 79% of the FRP retrievals have a difference <50%, with 39% <20%. Considering that almost exactly simultaneous MODIS FRP measures of the same fire pixel indicate an FRP uncertainty of 27% (1σ) for MODIS alone (Freeborn et al., 2014), the degree of AHI to MODIS FRP agreement seems very reasonable and comparable to that between MODIS and the LSA SAF Meteosat SEVIRI FRP product (Roberts et al., 2015).

MTSAT and MODIS matchups from Feb. 2009 are also shown on Fig. 7. Due to relatively fewer fires being present at this time compared to June 2015, to the reduced temporal resolution of MTSAT compared to AHI, and to the aforementioned problem MTSAT has detecting fires against warm backgrounds, there were far fewer MTSAT-to-MODIS matchups than there were AHI-to-MODIS. Furthermore, MTSAT fire clusters were only used when all constituent fire pixels were unsaturated (BT_{MWIR} < 320 K). Despite the limited number of matchups, the FRP data of MTSAT and MODIS still show a reasonable correlation (r^2 = 0.74) and slope of the linear best fit (0.89), with a bias slightly higher than AHI to MODIS (14 MW; 6%), though a smaller standard deviation (86 MW, 33%). All matchups have an FRP difference <50%, with 46% <20%. Overall MTSAT shows a strong degree of agreement with MODIS provided its data are unsaturated, but the performance in terms of active fire detection is far worse than that of AHI.

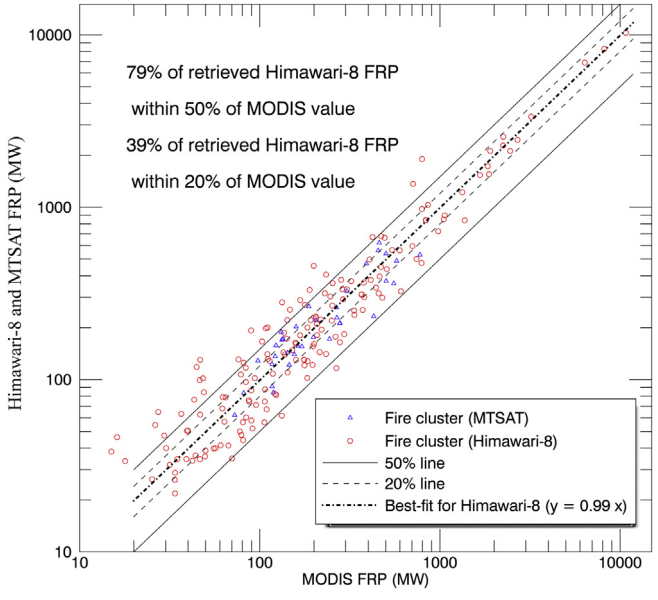

Fig. 7. Per-fire FRP intercomparison made using FRP retrievals from the MTSAT imager, Himawari-8 AHI and MODIS. Matching MODIS and AHI data are from June 2015, and those from MTSAT and MODIS from Feb 2009. Each symbol represents data from a single active fire cluster, representing a spatially contiguous or near-continuous group of active fire pixels detected near simultaneously by both sensors. In total, 168 AHI fire clusters and 35 MTSAT fire clusters are used, with the latter particularly low in part because the much higher active fire omission error and MWIR channel saturation of that sensor (Table 3) makes it more challenging to identify suitable matchups (see main text).

5.2.3.2. Per-area FRP intercomparison. When AHI and MODIS simultaneously detect the same active fire, AHI provides a reliable FRP measure (Fig. 7), but AHI does miss 66% of the MODIS-R fire pixels (Section 5.2.2) – primarily those at or below the nominal AHI FRP detection limit (Fig. 5). Many of these undetected low FRP fires are likely to be due to agricultural residue burning, which represents a very substantial fraction of fire activity in Asia (Zhang et al., 2012; Zhang et al., 2015; Li et al., 2016), and this 'small fire' detection bias demonstrably leads to significant regional-scale FRP underestimation when using AHI (Fig. 8) as well as other geostationary sensors (e.g. Freeborn et al., 2009; Roberts et al., 2015; Wooster et al., 2015; Xu et al., 2010). Of course, MODIS only observes an area a few times per day, whereas AHI provides almost continuous observations opportunities, and Wooster et al. (2015) show that in the case of the LSA SAF Meteosat SEVIRI active fire data, most fires missed by the geostationary observation made at the time of the MODIS overpass are detected by the geostationary data at other points during the fires lifetime.

Freeborn et al. (2014) used the ratio between the total cumulative FRP ($\sum$FRP) measured simultaneously in the same geographic region by Meteosat SEVIRI and by MODIS to quantify the impact of the (primarily low-FRP) fires not detected by the former. We found the ratio of $\sum FRP_{AHI}$ to $\sum FRP_{MODIS}$ as 0.54, and $\sum FRP_{MTSAT}$ to $\sum FRP_{MODIS}$ as 0.31, with the former higher because of AHI's lower active fire detection omission error compared to MTSAT (Section 5.2.2) and because of the MWIR band saturation problems of MTSAT that result in FRP underestimation for stronger fires (Fig. 2). Hyer et al. (2013) already report that MTSAT data processed with the WF_ABBA active fire detection algorithm developed show a rather lower overall active fire detection efficiency, particularly around local noon due to MWIR channel saturation. Our work confirms MTSAT's tendency to miss very many fires that MODIS can detect, even if they are burning rather strongly, but we see significant improvement in this situation using AHI.

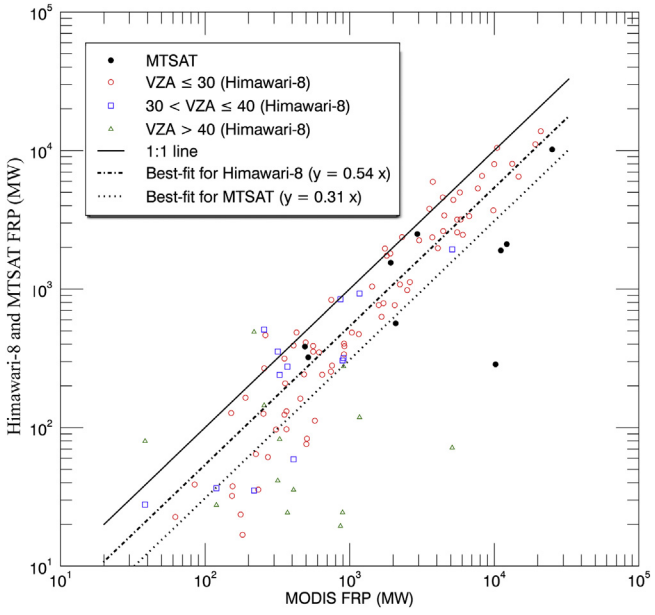

Fig. 8. Comparison of total FRP measured in spatially matched regions imaged contemporaneously by Himawari-8 AHI and MODIS throughout June 2015 at a MODIS scan angle of less than ±30°. The least squares linear best-fit passing through the origin is shown (dot dash line), and AHI tends to generally underestimate total FRP primarily due to the non-detection of most fires burning below its minimum FRP detection limit.

5.2.4. FRP frequency magnitude analysis

Following the kind of analysis shown in Freeborn et al. (2011) for Meteosat SEVIRI, Fig. 9 shows the frequency of all active fire pixels of different FRPs recorded by AHI and by MODIS over the AHI full disk region in June 2015, along with those detected by both sensors almost simultaneously. The Collection 5 MOD14/MYD14 MODIS active fire products have a minimum FRP detection limit of ~8–10 MW, and in most fire affected regions there are typically many more fire pixels approaching this limit than there are than higher FRP fire pixels. AHI can detect some fire pixels approaching the FRP detection limit of MODIS, but frequency of detection peaks at ~30 MW. Below this, AHI fails to detect many fire pixels that MODIS can detect, due to the larger pixel areas. Above 40 MW, the frequency distributions of the near simultaneous AHI and MODIS data are very similar, confirming that the majority of AHI active fire pixel omissions are low FRP (Fig. 5). Also demonstrated is the fact that AHI does not show an upper FRP breakpoint, such as the one exhibited by SEVIRI (Roberts and Wooster, 2008; Freeborn et al., 2011), largely because MTSAT's 400 K MWIR band maximum measurable signal (c.f. 335 K for SEVIRI) largely prevents saturation. In data of June 2015, only 0.06% (173 pixels) of the AHI-detected active fire pixels are saturated.

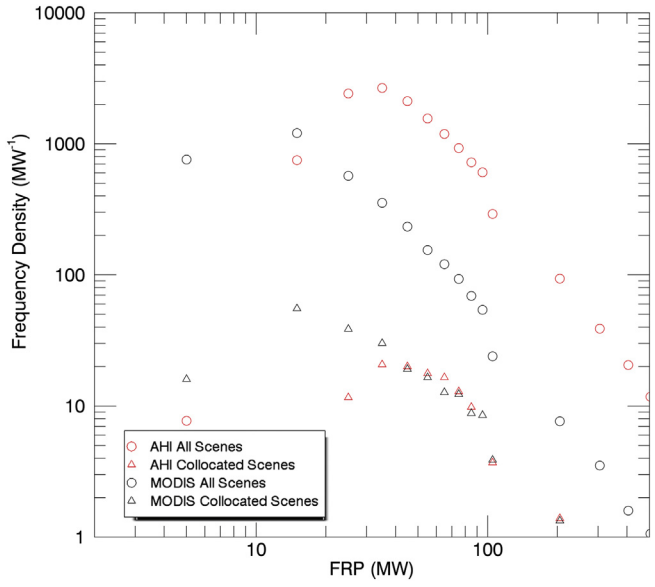

Fig. 9. Frequency density vs. FRP magnitude distributions of active fire pixels detected by MODIS and Himawari-8 AHI, constructed from (i) the number of active fire pixels detected by all scenes collected in June 2015, and (ii) the number of those in only collocated scenes taken within ±6 min of one another. Fire pixels with an FRP > 500 MW are not shown due to their rarity.

6. Asian and Australian fire activity records

Section 5's performance assessment indicates that Himawari-8 AHI offers major advantages over FY-2 and MTSAT for geostationary active fire detection and FRP characterisation, and we now turn our attention to briefly demonstrating the utility of the AHI fire radiative power retrievals. Future work will exploit longer datasets to build upon the limited analyses presented herein.

6.1. Large scale spatial patterns

Fig. 10 summarises MODIS' active fire data of June 2015 at 0.5° resolution, and compares it side-by-side to that of AHI. Substantial burning across parts of Asia is common at this time (Li et al., 2016), with similar patterns seen from the two sensors. Grid cells showing high total FRP result from either large numbers of active fire pixels, individual fires of particularly high FRP, or persistent or re-occurring fires in the same grid over the month. Areas showing concentrations of high FRP grid cells include eastern China, resulting from numerous agricultural residue fires (Randerson et al., 2012; Zhang et al., 2015; Li et al., 2016), southeast Asia which hosts a mixture of agricultural burning, forest clearance and peatland fires (Gaveau et al., 2013), and northern Australia that sees savannah burns (Williams et al., 1998).

Some clear differences between the AHI- and MODIS-derived FRP records can also be seen, for example in northern India where Chand et al. (2007) reported heavy burning in Uttaranchal State, and in Russia (Western from 120°E) and Kazakhstan, where MODIS typically shows increased fire signatures compared to AHI – probably related to the large view zenith angle of AHI at these higher latitudes (with AHI pixel areas >4× larger than at the SSP).

6.2. Diurnal cycles

The most unique aspect of geostationary imaging satellites is their ability to provide almost continuous observations (cloud cover permitting), and thus highly detailed temporal information on the daily cycle of fire activity (Roberts et al., 2009a, 2009b). Fig. 11 shows the hourly mean FRP recorded in June 2015 across the AHI full disk in the three main regional land cover types (based on the IGBP 1 km resolution land cover map; Loveland and Belward, 1997). Savannah fires are generally responsible for the highest total FRP, whilst agriculture typically shows the least - apart from on 11th June 2015 when an anomalously large group of crop residue fires are observed in eastern China (Fig. 11c), discussed further below. Fig. 11 also demonstrates that forest burning apparently showed a significant increase in the second half of June, mostly related to fires in Indonesia and Australia.

In Fig. 11, the middle and right columns show the monthly mean and standard deviation of FRP and normalised diurnal cycle (DC), calculated using the approach of Roberts et al. (2009a, 2009b). Smooth cycles are seen for each landcover, with a nighttime minimum, a daytime peak occurring around 13:00 h local solar time (though the mean DC of agriculture peaks slightly earlier), and generally weakening afternoon fire

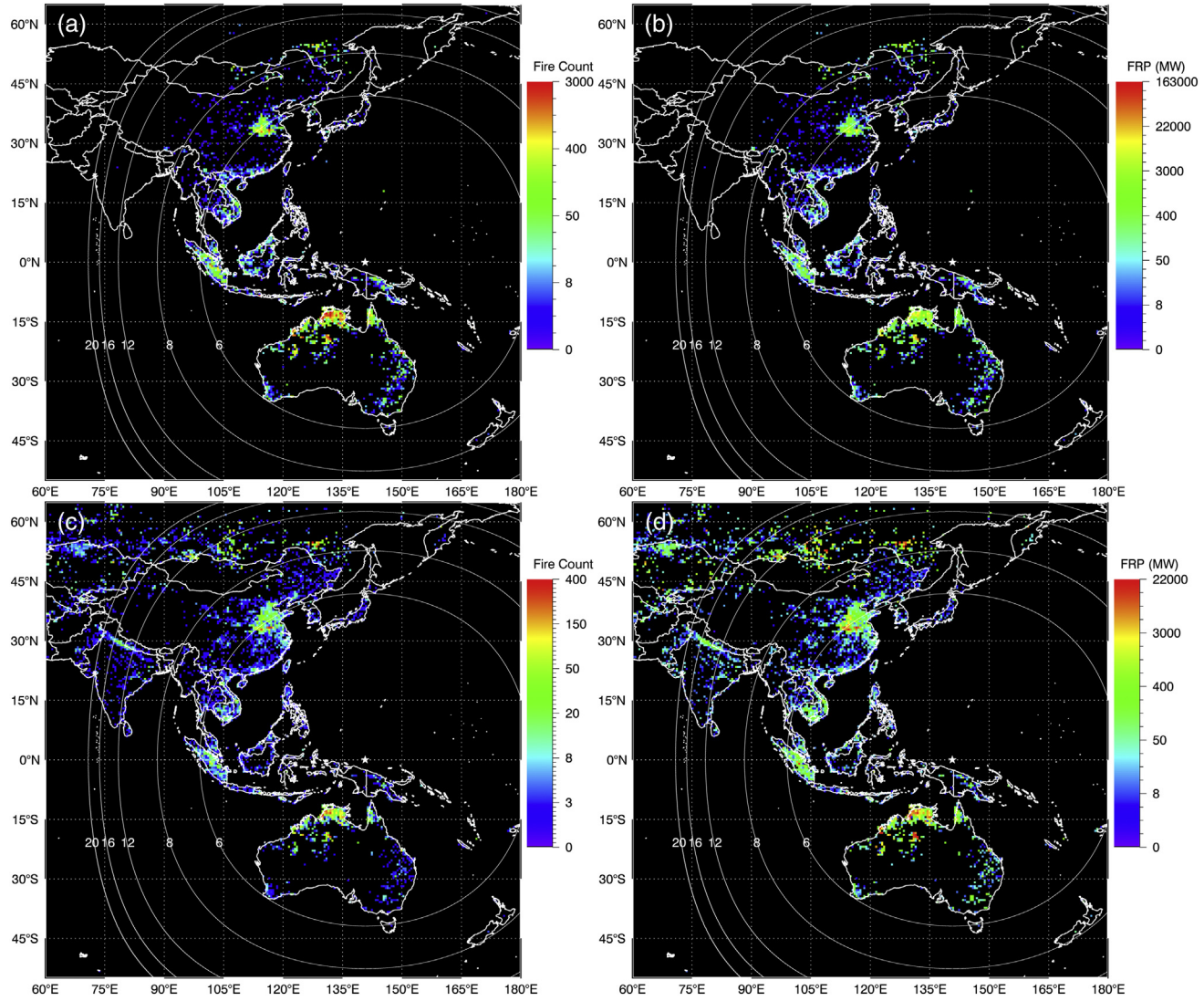

Fig. 10. Total fire count and total FRP of actively burning fires detected within 0.5° grid cells in June 2015 using all observation opportunities from AHI and MODIS. (a) Fire count from Himawari-8 AHI; (b) FRP from AHI; (c) Fire count from MODIS; (d) FRP from MODIS. AHI sub-satellite point is indicated by the white star above Papua New Guinea/West Papua, whilst the white circles indicate the pixel area variations (labels are area in km^2).

activity. Whilst savannah shows a continuously decreasing trend into the night, forest and agriculture show small local FRP peaks around 20:00–21:00 h local solar time, possibly due to timings of anthropogenic burning practices in areas where the authorities formally outlaw burning and thus some fires are purposely conducted after nightfall. Also, the standard deviation shown in the diurnal cycle (DC) plots is significantly smaller and more consistent across the day than is the standard deviation of FRP. Agriculture shows the largest variability and savannah the smallest, perhaps due to agricultural fires bring solely anthropically-driven.

Overall, the diurnal cycles in Fig. 11 for Asia and Australia appear broadly similar to those reported by Roberts et al. (2009a, 2009b) over Africa for the same landcovers. The peaks around 13:00 h local solar time seem a little earlier than the 13:00 h (Kalimantan) to 15:00 h (Northern Australia) peaks reported by Giglio (2007), though we have used only a single month of AHI data compared to the seven years of MODIS and TRMM VIRS data in Giglio (2007), and have focused over the full AHI disk rather than regionally as did Giglio (2007). As the AHI active fire data record lengthens, we will perform more nuanced analyses to determine whether the near continuous observations provided from geostationary orbit do indeed alter conclusions so-far made largely from polar orbiters.

Fig. 12 provides more detail on the diurnal variation in FRP for 11th June 2015 in Henan province (North China Plain), which Fig. 11c shows demonstrates an unusually large FRP peak. AHI and MODIS both indicate its existence, but the former shows much more temporal detail and captures the FRP maximum just before 14:00 h local solar time, whereas the sparser MODIS record provides an artificial peak time of at 11:10 h (as shown in Fig. 3a, where multiple fires are clearly seen) due to the early afternoon Aqua MODIS overpass recording the area at a very large view zenith angle and thus coarse pixel area (6.4 km^2; larger than the AHI pixels) whilst resulted in many fire pixels remaining undetected by MODIS. MODIS' difficulties in detecting fires at larger view angles are detailed in e.g. Freeborn et al. (2011). Clearly, when using polar obiter data alone (e.g. Vermote et al., 2009) care must be taken not to allow far-off nadir observations to introduced unwanted impacts (as identified by Freeborn et al., 2011), not only regarding FRP magnitude but also the timing of diurnal peaks. This clearly demonstrates

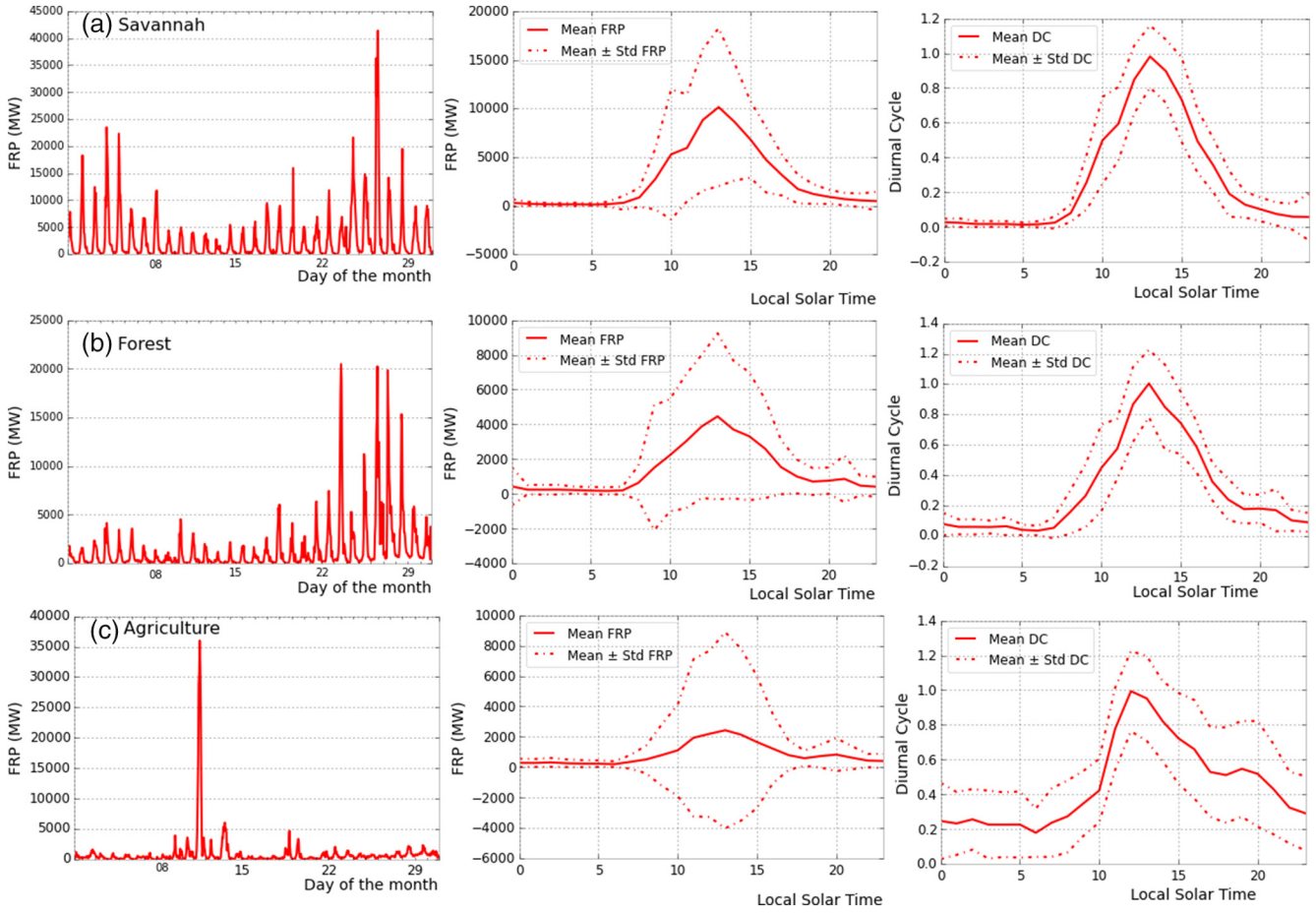

Fig. 11. Active fire information derived across the Himawari-8 AHI full disk in June 2015 for the three key IGBP land cover types; (a) Savannah, (b) Forest, and (c) Agriculture. Shown are (left column) hourly mean FRP, (middle) monthly mean ($\pm 1\sigma$) of FRP, and (right) normalised diurnal cycle. Local solar time is shown rather than UTC. Fires typically peak in the early afternoon, and activity is generally low at night.

the value of geostationary observations, and also very likely additional benefits can be gained by combining them with polar orbiting data to better understand the fire diurnal cycle (e.g. Freeborn et al., 2009; Freeborn et al., 2011; Roberts et al., 2011; Andela et al., 2015). Such diurnal cycle information remains important when linking fire emissions estimates to atmospheric transport models (e.g. Wang et al., 2006) and in converting 'snapshot' FRP measures from sensors such as MODIS into estimates of temporally integrated FRE (e.g. Vermote et al., 2009; Andela et al., 2015).

7. Summary and conclusions

We have developed algorithms for active fire detection and fire radiative power (FRP) retrieval across Asia and Australia, based on data

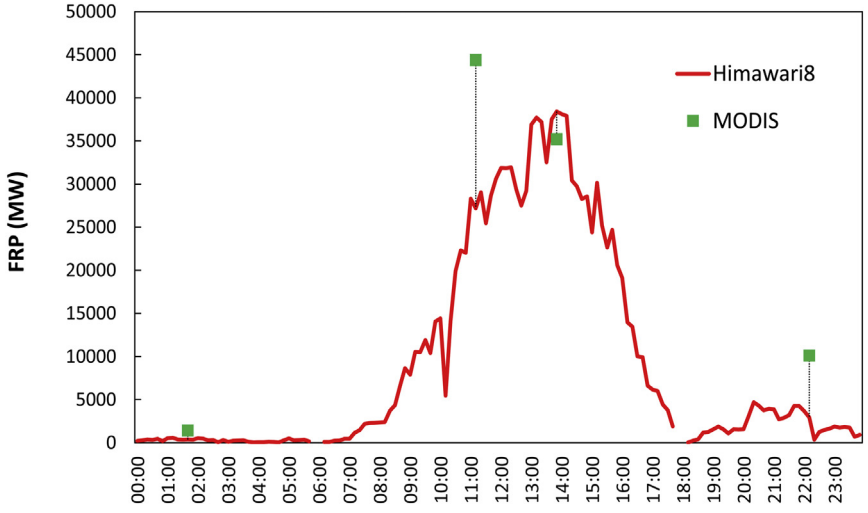

Fig. 12. Diurnal cycle of agricultural residue burning fires in Eastern China on 11th June 2015, whose signatures were recorded by Himawari-8 AHI and MODIS. Note this study area is the same as the map inserted on the top left of the Fig. 3 as indicated by the red rectangle.

from the FY-2 S-VISSR, MTSAT imager and Himawari-8 AHI, the geostationary Fire Thermal Anomaly (FTA) active fire detection algorithm of Roberts and Wooster (2008) and Wooster et al. (2015), the cloud masking procedures of Xu et al. (2010), and the MIR radiance method of FRP retrieval (Wooster et al., 2003, 2005, 2013). For the first time we have intercompared active fire data generated from each of these geostationary data sources, and compared each to simultaneous active fire data from MODIS. FY-2 misses almost all active fires, mainly due to poor MWIR channel image quality and a low spatial resolution (5 km at the SSP). MTSAT (SSP spatial resolution of 4 km) shows a reasonable ability to detect active fires and retrieve their FRP, as long as ambient background temperatures are low enough and the fire not too large so that MWIR channel saturation is avoided. Himawari-8 offers much better capability than the other two sensors, with an ~8% active fire detection error of commission and ~66% of error of omission compared to MODIS, a performance similar to the FTA algorithm applied to data from Meteosat SEVIRI and the GOES imager (Roberts and Wooster, 2008; Roberts et al., 2015; Xu et al., 2010). When AHI and MODIS detect the same fire at the same time we see a very low 3 MW bias between their FRP retrievals, though regionally AHI underestimates FRP by around 50% compared to the simultaneous MODIS view because it cannot easily detect the (rather common) fires whose FRP lies below ~40 MW.

We have used AHI to provide the first genuine diurnal cycle derivation for Asian and Australian fires available from a geostationary satellite. Diurnal patterns are similar to those of the same landcovers found in Africa (e.g. Roberts et al., 2009a, 2009b), with early afternoon peaks fairly comparable but not identical to those reported by Giglio (2007) using data from polar orbiters (MODIS and TRMM). Despite limitations imposed by their relatively coarse spatial resolution, the high temporal resolution offered by geostationary satellites is a key advantage for active fire applications, and highly valuable when driving smoke emissions estimates for use in atmospheric transport models (Reid et al., 2009; Baldassarre et al., 2015; Roberts et al., 2015). We find that the Himawari AHI system offers major advantages over the prior geostationary systems operating over Asia, and we expect that the scheme detailed herein will enable real-time processing of AHI data to join that of GOES (Xu et al., 2010) and Meteosat SEVIRI (Wooster et al., 2015) and becoming an important component of a consistent global geostationary FRP characterisation system. Furthermore, since the Advanced Baseline Imager (ABI) sensor onboard the forthcoming GOES-R spacecraft is extremely similar to AHI (Schmit et al., 2005), the optimised FTA algorithm evaluated here should be easily applicable to the GOES-R mission.

Acknowledgements

We wish to thank to Dr. Takeshi Murata of the National Research and Development Institute of Information and Communications Technology Integrated Data System Research Development Office, and for use of the National Institute of Information and Communications Technology (NICT) Science Cloud who enabled access to Himawari-8 data. FY-2 data was kindly provided by Professor Liu Cheng of the Chinese Meteorological Administration (CMA), and MTSAT data from Professor Wei Fan in the East China Sea Fisheries Research Institute. MODIS data are courtesy of NASA, and we wish to also acknowledge all the National Space Agencies and related organisations whose work made the collection and use of these datasets possible. The parts of this work dealing with MTSAT and FY2 were supported by funding from Innovation China UK (KCL09), with development of the Himawari (H8) algorithm by the UK National Center for Earth Observation (NCEO-King's), and with the validation of the H8 outputs with funding from the European Union. That material is being communicated/published in the name of the Commission, and the Commission is not responsible for any use that may be made of the information. We thank the four reviewers for their constructive comments and suggestions.

References

Andela, N., Kaiser, J.W., Van der Werf, G.R., Wooster, M.J., 2015. New fire diurnal cycle characterizations to improve fire radiative energy assessments made from MODIS observations. Atmos. Chem. Phys. 15, 8831–8846.

Baldassarre, G., Pozzoli, L., Schmidt, C.C., Unal, A., Kindap, T., Menzel, W.P., Whitburn, S., Coheur, P.F., Kavgaci, A., Kaiser, J.W., 2015. Using SEVIRI fire observations to drive smoke plumes in the CMAQ air quality model: a case study over Antalya in 2008. Atmos. Chem. Phys. 15 (14), 8539–8558.

Bessho, K., Date, K., Hayashi, M., Ikeda, A., Imai, T., Inoue, H., Kumagai, Y., Miyakawa, T., Murata, H., Ohno, T., 2016. An introduction to Himawari-8/9—Japan's new-generation geostationary meteorological satellites. J. Meteorol. Soc. Japan 94, 151–183.

Bowman, D.M.J.S., 2000. Australian Rainforests: Islands of Green in a Land of Fire. Cambridge University Press.

Chand, T.K., Badarinath, K.V.S., Murthy, M.S.R., Rajshekhar, G., Elvidge, C.D., Tuttle, B.T., 2007. Active forest fire monitoring in Uttaranchal State, India using multi-temporal DMSP-OLS and MODIS data. Int. J. Remote Sens. 28 (10), 2123–2132.

Engel, C.B., Lane, T.P., Reeder, M.J., Rezny, M., 2013. The meteorology of Black Saturday. Q. J. R. Meteorol. Soc. 139, 585–599.

Freeborn, P.H., Wooster, M.J., Roberts, G., 2011. Addressing the spatiotemporal sampling design of MODIS to provide estimates of the fire radiative energy emitted from Africa. Remote Sens. Environ. 115, 475–489.

Freeborn, P.H., Wooster, M.J., Roberts, G., Xu, W., 2014. Evaluating the SEVIRI fire thermal anomaly detection algorithm across the Central African Republic using the MODIS active fire product. Remote Sens. 6, 1890–1917.

Freeborn, P.H., Wooster, M.J., Roberts, G., Malamud, B.D., Xu, W.D., 2009. Development of a virtual active fire product for Africa through a synthesis of geostationary and polar orbiting satellite data. Remote Sens. Environ. 113, 1700–1711.

Gaveau, D.L., Kshatriya, M., Sheil, D., Sloan, S., Molidena, E., Wijaya, A., Wich, S., Ancrenaz, M., Hansen, M., Broich, M., Guariguata, M.R., 2013. Reconciling forest conservation and logging in Indonesian Borneo. PloS One 8 (8), p.e69887.

Giglio, L., Descloitres, J., Justice, C.O., Kaufman, Y.J., 2003. An enhanced contextual fire detection algorithm for MODIS. Remote Sens. Environ. 87 (2), 273–282.

Giglio, L., 2007. Characterization of the tropical diurnal fire cycle using VIRS and MODIS observations. Remote Sens. Environ. 108, 407–421.

Giglio, L., Schroeder, W., Justice, C.O., 2016. The collection 6 MODIS active fire detection algorithm and fire products. Remote Sens. Environ. 178, 31–41.

Giglio, L., Van der Werf, G.R., Randerson, J.T., Collatz, G.J., Kasibhatla, P., 2006. Global estimation of burned area using MODIS active fire observations. Atmos. Chem. Phys. 6, 957–974.

Guo, Q., Li, X.Y., Chen, G.L., 2009. On-orbit Mtf evaluation for thermal infrared band of Fy-2 satellite and its application in image quality improvements. J. Infrared and Millimeter Waves 28, 335–341.

Huijnen, V., Wooster, M.J., Kaiser, J.W., Gaveau, D.L.A., Flemming, J., Parrington, M., Inness, A., Murdiyarso, D., Main, B., van Weele, M., 2016. Fire carbon emissions over maritime Southeast Asia in 2015 largest since 1997. Sci. Report. 6, 26886.

Hyer, E.J., Reid, J.S., Prins, E.M., Hoffman, J.P., Schmidt, C.C., Miettinen, J.I., Giglio, L., 2013. Patterns of fire activity over Indonesia and Malaysia from polar and geostationary satellite observations. Atmos. Res. 122, 504–519.

JMA, 2014. JMA/MSC: Himawari-8/9. Japan Meteorological Agency (Retrieved 7 October 2015).

Johnston, F., Hanigan, I., Henderson, S., Morgan, G., Bowman, D., 2011. Extreme air pollution events from bushfires and dust storms and their association with mortality in Sydney, Australia 1994–2007. Environ. Res. 111, 811–816.

Kurihara, Y., Murakami, H., Kachi, M., 2016. Sea surface temperature from the new Japanese geostationary meteorological Himawari-8 satellite. Geophys. Res. Lett. 43, 1234–1240.

Li, J., Bo, Y., Xie, S., 2016. Estimating emissions from crop residue open burning in China based on statistics and MODIS fire products. J. Environ. Sci. 44, 158–170.

Loveland, T., Belward, A., 1997. The IGBP-DIS global 1km land cover data set, DISCover: first results. Int. J. Remote Sens. 18, 3289–3295.

Randerson, J.T., Chen, Y., Werf, G.R., Rogers, B.M., Morton, D.C., 2012. Global burned area and biomass burning emissions from small fires. J. Geophys. Res. Biogeosci. 117 (G4).

Reid, J.S., Hyer, E.J., Johnson, R.S., Holben, B.N., Yokelson, R.J., Zhang, J., Campbell, J.R., Christopher, S.A., Di Girolamo, L., Giglio, L., Holz, R.E., Kearney, C., Miettinen, J., Reid, E.A., Turk, F.J., Wang, J., Xian, P., Zhao, G., Balasubramanian, R., Chew, B.N., Janjai, S., Lagrosas, N., Lestari, P., Lin, N.-H., Mahmud, M., Nguyen, A.X., Norris, B., Oanh, N.T.K., Oo, M., Salinas, S.V., Welton, E.J., Liew, S.C., 2013. Observing and understanding the Southeast Asian aerosol system by remote sensing: An initial review and analysis for the Seven Southeast Asian Studies (7SEAS) program. Atmos. Res. 122, 403–468.

Reid, J.S., Hyer, E.J., Prins, E.M., Westphal, D.L., Zhang, J.L., Wang, J., Christopher, S.A., Curtis, C.A., Schmidt, C.C., Eleuterio, D.P., Richardson, K.A., Hoffman, J.P., 2009. Global monitoring and forecasting of biomass-burning smoke: description of and lessons from the fire locating and modeling of burning emissions (FLAMBE) program. Ieee Journal of Selected Topics in Applied Earth Observations and Remote Sensing. 2, pp. 144–162.

Roberts, G., Wooster, M., Freeborn, P.H., Xu, W., 2011. Integration of geostationary FRP and polar-orbiter burned area datasets for an enhanced biomass burning inventory. Remote Sens. Environ. 115, 2047–2061.

Roberts, G., Wooster, M.J., Lagoudakis, E., 2009a. Annual and diurnal African biomass burning temporal dynamics. Biogeosciences 6, 849–866.

Roberts, G., Wooster, M.J., Lagoudakis, E., Freeborn, P., Xu, W., 2009b. Continental Africa biomass burning temporal dynamics derived from MSG SEVIRI. 2009 Ieee International Geoscience and Remote Sensing Symposium. 1–5, pp. 1458–1461.

Roberts, G., Wooster, M.J., Perry, G.L.W., Drake, N., Rebelo, L.M., Dipotso, F., 2005. Retrieval of biomass combustion rates and totals from fire radiative power observations:

application to southern Africa using geostationary SEVIRI imagery. J. Geophys. Res.-Atmos. 110.
Roberts, G.J., Wooster, M.J., 2008. Fire detection and fire characterization over Africa using Meteosat SEVIRI. IEEE Trans. Geosci. Remote Sens. 46, 1200–1218.
Roberts, G., Wooster, M.J., Xu, W., Freeborn, P.H., Morcrette, J.-J., Jones, L., Benedetti, A., Jiangping, H., Fisher, D., Kaiser, J.W., 2015. LSA SAF Meteosat FRP products – part 2: evaluation and demonstration for use in the Copernicus Atmosphere Monitoring Service (CAMS). Atmos. Chem. Phys. 15, 13241–13267.
Roy, D.P., Boschetti, L., Justice, C.O., Ju, J., 2008. The collection 5 MODIS burned area product—global evaluation by comparison with the MODIS active fire product. Remote Sens. Environ. 112 (9), 3690–3707.
Schmit, T.J., Gunshor, M.M., Menzel, W.P., Gurka, J.J., Li, J., Bachmeier, A.S., 2005. Introducing the next-generation Advanced Baseline Imager on goes-R. Bull. Am. Meteorol. Soc. 86, 1079–1096.
Stephenson, C., Handmer, J., Betts, R., 2013. Estimating the economic, social and environmental impacts of wildfires in Australia. Environmental Hazards-Human and Policy Dimensions. 12, pp. 93–111.
Van Der Werf, G.R., Randerson, J.T., Collatz, G.J., Giglio, L., Kasibhatla, P.S., Arellano, A.F., Olsen, S.C., Kasischke, E.S., 2004. Continental-scale partitioning of fire emissions during the 1997 to 2001 El Nino/La Nina period. Science 303, 73–76.
Van der Werf, G.R., Randerson, J.T., Giglio, L., Collatz, G.J., Mu, M., Kasibhatla, P.S., Morton, D.C., DeFries, R.S., Jin, Y., van Leeuwen, T.T., 2010. Global fire emissions and the contribution of deforestation, savanna, forest, agricultural, and peat fires (1997–2009). Atmos. Chem. Phys. 10, 11707–11735.
Vermote, E., Ellicott, E., Dubovik, O., Lapyonok, T., Chin, M., Giglio, L., Roberts, G.J., 2009. An approach to estimate global biomass burning emissions of organic and black carbon from MODIS fire radiative power. J. Geophys. Res.-Atmos. 114.
Wang, J., Christopher, S.A., Nair, U.S., Reid, J.S., Prins, E.M., Szykman, J., Hand, J.L., 2006. Mesoscale modeling of Central American smoke transport to the United States: 1."Top-down" assessment of emission strength and diurnal variation impacts. J. Geophys. Res. Atmos. 111 (D5).
Wolf, R., Just, D., 1999. LRIT/HRIT Global Specification. Coordination Group for Meteorological Satellites.
Williams, R., Gill, A., Moore, P., 1998. Seasonal changes in fire behaviour in a tropical savanna in northern Australia. Int. J. Wildland Fire 8, 227–239.
Wooster, M.J., Perry, G.L.W., Zoumas, A., 2012. Fire, drought and El Niño relationships on Borneo (Southeast Asia) in the pre-MODIS era (1980–2000). Biogeosciences 9, 317–340.
Wooster, M.J., Roberts, G., Freeborn, P.H., Xu, W., Govaerts, Y., Beeby, R., He, J., Lattanzio, A., Mullen, R., 2015. Meteosat SEVIRI fire radiative power (FRP) products from the Land Surface Analysis Satellite Applications Facility (LSA SAF) – part 1: algorithms, product contents and analysis. Atmos. Chem. Phys. Discuss. 15, 15831–15907.
Wooster, M.J., Roberts, G., Perry, G.L.W., Kaufman, Y.J., 2005. Retrieval of biomass combustion rates and totals from fire radiative power observations: FRP derivation and calibration relationships between biomass consumption and fire radiative energy release. J. Geophys. Res.-Atmos. 110, 1–24.
Wooster, M.J., Roberts, G., Smith, A.M.S., Johnston, J., Freeborn, P., Amici, S., Hudak, A.T., 2013. Thermal remote sensing of active vegetation fires and biomass burning events. In: Kuenzer, C., Dech, S. (Eds.), Thermal Infrared Remote Sensing: Sensors, Methods, Applications. Springer Netherlands, Dordrecht, pp. 347–390.
Wooster, M.J., Zhukov, B., Oertel, D., 2003. Fire radiative energy for quantitative study of biomass burning: derivation from the BIRD experimental satellite and comparison to MODIS fire products. Remote Sens. Environ. 86, 83–107.
Xu, W., Wooster, M.J., Roberts, G., Freeborn, P., 2010. New GOES imager algorithms for cloud and active fire detection and fire radiative power assessment across North, South and Central America. Remote Sens. Environ. 114, 1876–1895.
Zhang, T.R., Wooster, M.J., Green, D.C., Main, B., 2015. New field-based agricultural biomass burning trace gas, PM2.5, and black carbon emission ratios and factors measured in situ at crop residue fires in eastern China. Atmos. Environ. 121, 22–34.
Zhang, X., Kondragunta, S., Ram, J., Schmidt, C., Huang, H.C., 2012. Near-real-time global biomass burning emissions product from geostationary satellite constellation. J. Geophys. Res. Atmos. 117 (D14).
Zhukov, B., Lorenz, E., Oertel, D., Wooster, M., Roberts, G., 2006. Spaceborne detection and characterization of fires during the bi-spectral infrared detection (BIRD) experimental small satellite mission. (2001–2004). Remote Sens. Environ. 100 (1), 29–51.